



Characterization and evaluation of double perovskites $\text{LnBaCoFeO}_{5+\delta}$ ($\text{Ln} = \text{Pr}$ and Nd) as intermediate-temperature solid oxide fuel cell cathodes

Fangjun Jin^a, Huawei Xu^a, Wen Long^a, Yu Shen^{a,b}, Tianmin He^{a,*}

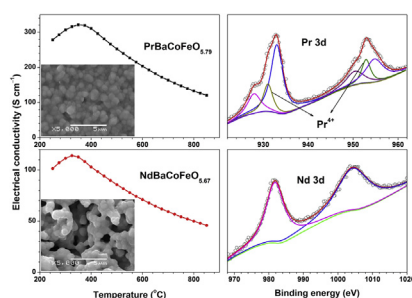
^a Key Laboratory of Physics and Technology for Advanced Batteries, Ministry of Education, College of Physics, Jilin University, Changchun 130012, PR China

^b School of Materials Science and Engineering, Changchun University of Science and Technology, Changchun 130022, PR China

HIGHLIGHTS

- Double perovskites $\text{LnBaCoFeO}_{5+\delta}$ ($\text{Ln} = \text{Pr}$ and Nd) with near metal stoichiometry were prepared by the modified sol–gel method.
- We comparatively studied structures and properties of double perovskites $\text{LnBaCoFeO}_{5+\delta}$ as IT-SOFC cathodes.
- Mixed valence states of $\text{Pr}^{3+}/\text{Pr}^{4+}$, $\text{Co}^{3+}/\text{Co}^{4+}$ and $\text{Fe}^{3+}/\text{Fe}^{4+}$ coexisted in the $\text{PrBaCoFeO}_{5+\delta}$ oxide.
- Substitution of Fe for Co reduced the TECs of the $\text{LnBaCoFeO}_{5+\delta}$ compared to undoped $\text{LnBaCo}_2\text{O}_{5+\delta}$ ($\text{Ln} = \text{Pr}$ and Nd).
- $\text{LnBaCoFeO}_{5+\delta}$ as IT-SOFC cathodes on LSGM electrolyte exhibited good electrochemical performance.

GRAPHICAL ABSTRACT



ARTICLE INFO

Article history:

Received 7 April 2013

Received in revised form

30 May 2013

Accepted 31 May 2013

Available online 11 June 2013

Keywords:

Solid oxide fuel cell

Double perovskite cathode

X-ray photoelectron spectroscopy

Electrical conductivity

Thermal expansion

Electrochemical performance

ABSTRACT

Double perovskites $\text{LnBaCoFeO}_{5+\delta}$ ($\text{Ln} = \text{Pr}$ and Nd , PBCF and NBCF) are comparatively investigated as potential cathode materials for intermediate-temperature solid oxide fuel cells (IT-SOFCs). $\text{LnBaCoFeO}_{5+\delta}$ materials are chemically compatible with $\text{La}_{0.9}\text{Sr}_{0.1}\text{Ga}_{0.8}\text{Mg}_{0.2}\text{O}_{3-\delta}$ (LSGM) electrolyte at temperatures below 1000 °C. Fe and Co ions in $\text{LnBaCoFeO}_{5+\delta}$ exist in two oxidation states, 3+ and 4+. Pr ions are found in PBCF mostly as Pr^{3+} . Thermal expansion coefficients (TECs) of PBCF and NBCF are 21.0×10^{-6} and $19.5 \times 10^{-6} \text{ K}^{-1}$, respectively, between 30 and 1000 °C; these are lower than the TECs of undoped $\text{LnBaCo}_2\text{O}_{5+\delta}$. The best electrical conductivity for both materials is observed near 350 °C: 321 and 172 S cm^{-1} for PBCF and NBCF, respectively. Polarization resistances of PBCF and NBCF cathodes on LSGM electrolyte are 0.049 and $0.062 \Omega \text{ cm}^2$ at 800 °C, respectively. Maximum power densities of the single-cell with Ni/SDC as anode on a 0.3 mm-thick LSGM electrolyte reach 749 and 669 mW cm^{-2} for PBCF and NBCF cathodes at 800 °C, respectively. As cathodes for application in IT-SOFCs, the performance of PBCF and NBCF double perovskites is promising.

© 2013 Elsevier B.V. All rights reserved.

1. Introduction

Solid oxide fuel cells (SOFCs) are a type of electrochemical energy conversion devices and provide electrical power with high

* Corresponding author. Tel.: +86 431 85166112; fax: +86 431 85167827.
E-mail addresses: hetm@jlu.edu.cn, hly@mail.jlu.edu.cn (T. He).

efficiency and low pollution. So SOFCs are an important clean power generation technology in future sustainable energy systems. Generally, conventional SOFCs need to operate at around 1000 °C. Such a high operating temperature means the cost of a SOFC system is high, and performance degenerates easily. Therefore, SOFC operating temperature must be reduced in order to improve the long-term stability of its components and to reduce the costs of the SOFC system. In SOFCs, the cathode plays an important role in the electrochemical reduction of oxygen. In intermediate-temperature solid oxide fuel cells (IT-SOFCs), the decrease of operation temperature inevitably leads to a large overpotential and cathodic polarization loss [1–5]. Accordingly, it is necessary to develop a novel cathode material with high performance in the intermediate temperature range (600–800 °C). In recent years, cobalt-containing double perovskites $\text{LnBaCo}_2\text{O}_{5+\delta}$ ($\text{Ln} = \text{La, Pr, Nd, Sm, Gd, and Y}$) have been investigated as potential cathode materials for application in IT-SOFCs [6–16]. These double perovskite materials form a mixed ionic–electronic conductor, and their high oxygen permeation properties enable the three-phase boundary region to increase finitely, showing excellent electrochemical activities [17–19]. The $\text{LnBaCo}_2\text{O}_{5+\delta}$ oxides have Ln–O , Ba–O , and Co–O layers alternating along the c -axis; the ordering of the Ln–O and Ba–O layers determines the crystal structure and electrical property, the oxygen content δ varies within a wide range, and the alternating lanthanide and alkali–earth planes improve the oxygen transport properties [20–22]. Previous studies have shown the $\text{LnBaCo}_2\text{O}_{5+\delta}$ oxides to have unusually fast oxygen diffusion, oxygen surface exchange kinetics, and high electrical conductivity in the intermediate temperature range [18,19]. Many groups have also reported that $\text{LnBaCo}_2\text{O}_{5+\delta}$ ($\text{Ln} = \text{Pr, Nd, Sm, and Gd}$) materials reveal relatively low polarization resistance on $\text{La}_{0.9}\text{Sr}_{0.1}\text{Ga}_{0.8}\text{Mg}_{0.2}\text{O}_{3-\delta}$ (LSGM) electrolyte and high cell performance as IT-SOFC cathodes [13,14,16].

Although the $\text{LnBaCo}_2\text{O}_{5+\delta}$ double perovskites as novel cathode material have shown good surface exchange kinetics and catalytic activity, they have certain disadvantages: they have a high thermal expansion coefficient (TEC), the cobalt element in them is expensive; and they exhibit poor long-term chemical stability [6]. The larger TEC values for Co-containing double perovskite materials are closely related to the cobalt ion transition of the spin state from low spin ($t_{2g}^6 e_g^0$) to high spin ($t_{2g}^4 e_g^2$) and the lower bonding energy of the Co–O bond [22,23]. Partial substitution of Co with transition metals (Fe and Cu) in $\text{LnBaCo}_2\text{O}_{5+\delta}$ materials could potentially mitigate these disadvantages while maintaining satisfactory electrochemical activity [9,11,24–27]. For example, $\text{NdBaCo}_{2-x}\text{Fe}_x\text{O}_{5+\delta}$ cathodes showed a decreased TEC with increasing Fe content, from $21.5 \times 10^{-6} \text{ K}^{-1}$ for $x = 0.0$ to $2.0 \times 10^{-6} \text{ K}^{-1}$ for $x = 1.0$, while the maximum power density with the $x = 0.5$ cathode on the LSGM electrolyte reached about 570 mW cm^{-2} at 800 °C [9]. $\text{GdBaCoFeO}_{5+\delta}$ (GBCF) was also investigated as a potential cathode for IT-SOFCs, in which an SDC film cell with a GBCF cathode attained a maximum power density of 746 mW cm^{-2} at 650 °C [27].

Recently, Zhao et al. [11] reported that the double perovskite $\text{PrBaCo}_{2-x}\text{Fe}_x\text{O}_{5+\delta}$ had good stability at 700 °C in air containing 3% CO_2 , and it was chemically compatible with SDC electrolyte at 1000 °C. Zou et al. [12] showed that the electrical conductivity of $\text{PrBaCo}_{2-x}\text{Fe}_x\text{O}_{5+\delta}$ decreased with increasing Fe content, with the exception of the $x = 0.4$ sample, which showed an obvious jump in conductivity. The lowest cathode polarization resistance on SDC electrolyte was also observed for the $x = 0.4$ sample. Their studies showed that the partial substitution of Fe for Co either directly or indirectly improved the electrochemical performance of $\text{PrBaCo}_2\text{O}_{5+\delta}$. The emergence of these results compels us to further study the effect of Fe substitution for Co at equal mole amounts on structures and properties of $\text{LnBaCo}_2\text{O}_{5+\delta}$ ($\text{Ln} = \text{Pr and Nd}$).

In this paper, with an aim to reduce the TECs and cobalt element costs while maintaining good electrochemical performances, we synthesized the double perovskites $\text{PrBaCoFeO}_{5+\delta}$ (PBCF) and $\text{NdBaCoFeO}_{5+\delta}$ (NBCF) using combined ethylenediamine tetraacetic acid (EDTA) and citrate complexing sol–gel method (EDTA–citrate complexing method). The chemical states of PBCF and NBCF materials were characterized in detail by X-ray photoelectron spectroscopy (XPS). The effect of Fe substitution for Co on the structures, thermal expansion, and electrical behaviors of the PBCF and NBCF were investigated. The electrochemical performances of the PBCF and NBCF as cathodes on LSGM electrolyte were also evaluated.

2. Experimental

2.1. Sample preparation and cell fabrication

$\text{LnBaCoFeO}_{5+\delta}$ ($\text{Ln} = \text{Pr and Nd}$, PBCF and NBCF) powders were synthesized using EDTA–citrate complexing method. The stoichiometric mixture of Pr_6O_{11} , Nd_2O_3 , $\text{Ba}(\text{NO}_3)_2$, $\text{Fe}(\text{NO}_3)_3 \cdot 9\text{H}_2\text{O}$, and $\text{Co}(\text{NO}_3)_2 \cdot 6\text{H}_2\text{O}$ was weighed. Pr_6O_{11} and Nd_2O_3 were dissolved in nitric acid solution to form their respective nitrates. According to the cation stoichiometry of the precursors, these nitrates were mixed with citric acid and EDTA to form metal complex via inorganic polymerization reactions. The molar ratio of the EDTA/total metal ions/citric acid was 1:1:2 in the solution. Atramentous viscous gel was obtained by evaporating the excess water from the solution under stirring and heating. The resulting viscous gel was solidified with heating at 180 °C for 4 h. In order to remove organic matter, the spongy gel was ground in an agate mortar, and then the powders were slowly heated in air at 400 °C for 6 h and then at 900 °C for 10 h, respectively. Finally, the calcined powders were pelletized and subsequently sintered at 1150 °C for 10 h in air to obtain the single-phase materials with desired double perovskite structure. The LSGM powders were obtained from the glycine–nitrate process (GNP). Dense LSGM pellets 13 mm in diameter were prepared by uniaxial mold pressing of LSGM powders at 220 MPa and sintering at 1450 °C for 10 h in air [28]. Thickness was controlled to 0.3 mm by wet grinding the sintered pellets with waterproof abrasive paper. $\text{Ce}_{0.8}\text{Sm}_{0.2}\text{O}_{1.9}$ (SDC) was also synthesized by the GNP, followed by calcining at 800 °C for 2 h in air to form fluorite SDC powders.

Symmetrical cells of cathode/LSGM/cathode for impedance studies were prepared by screen printing cathode ink onto both sides of the LSGM electrolyte pellets. After drying, the samples were sintered at 900, 950, and 1000 °C for 2 h. Anode powder was prepared by thoroughly mixing NiO and SDC (65:35 weight ratio). Electrolyte-supported fuel cells, NiO-SDC/SDC/LSGM/cathode, were fabricated using 0.3-mm-thick LSGM pellets. The SDC interlayer was introduced between the electrolyte and the anode and sintered at 1300 °C for 1 h, the anode NiO-SDC was printed on the interlayer and sintered at 1250 °C for 4 h. The cathode was printed on the other side and sintered at 950 °C for 2 h. The silver current collector on both the anode and cathode surfaces was prepared by painting the pattern with silver paste. The cells were sealed onto the end of an alumina tube with silver paste to test cell performance.

2.2. Material characterization and cell test

The crystalline structure of the synthesized samples and chemical compatibility with the electrolyte were characterized with an X-ray diffractometer (Rigaku-D-Max γA , $\lambda = 0.15418 \text{ nm}$) at a scanning range of 20°–80° with a resolution of 0.02° per step at room temperature. Oxygen content in the $\text{LnBaCoFeO}_{5+\delta}$ samples was determined using the iodometric titration technique under a nitrogen atmosphere at room temperature. XPS measurements

were performed using a VG Scientific ESCALAB MK II X-ray photoelectron spectrometer. A monochromatized microfocused Al K α (1486.6 eV) radiation source was used. Experimental and analytical procedures were described elsewhere [29]. The TECs of the samples were measured between 30 and 1000 °C using a dilatometer (Netzsch DIL 402C), with an air-purge flow rate of 60 mL min⁻¹. A thermogravimetric analysis (TGA) curve was obtained using a thermal analyzer (HENVEN HCT-3) in air at a rate of 50 mL min⁻¹. The sample was measured between 30 and 1000 °C at a heating rate of 10 °C min⁻¹. A d.c. standard voltage/current generator (SB118) and a precision digital multimeter (PZ158A) were used to measure electrical conductivity of the samples with the van der Pauw method in temperature range 250–850 °C. A scanning electron microscope (SEM, JEOL JSM-6480LV) and energy dispersive X-ray spectroscopy (EDS, EDAX) were employed to inspect the microstructure and analyze the elemental composition of sample surface sintered at 1150 °C for 10 h.

To assess the electrochemical activity of the cathode, electrochemical impedance spectroscopy (EIS) of the symmetrical cells was conducted in air. The EIS and single-cell performance measurements were performed using an electrochemical analyzer (CHI604D, Chenhua) over the temperature range 600–800 °C. The EIS measurement ranged from 0.1 Hz to 100 kHz, and the a.c. signal amplitude was 10 mV. The single-cell performance test was conducted with the anode under dry H₂ and the cathode in ambient air at various temperatures. EIS of the single cell was performed using an electrochemical analyzer (IviumStat, Ivium) over temperature range 600–800 °C with frequency range from 0.1 Hz to 1 MHz under open-circuit conditions. The a.c. signal amplitude was 10 mV.

3. Results and discussion

3.1. Crystal structure and chemical compatibility

Fig. 1(a) and (b) shows the room temperature XRD patterns of PBCF and NBCF samples sintered at 1150 °C for 10 h. The samples prepared by EDTA–citrate complex method are well crystallized in a single-phase double perovskite oxide. The PBCF and NBCF double perovskites can be indexed in a tetragonal structure with the space group P4/mmm. In addition, the XRD patterns show a double peak at $2\theta \approx 32^\circ$ and 33° , which is an indication of the typical tetragonal structure of double perovskite [12]. This result is consistent with

findings from previous structural studies [9,30–32]. The unit-cell parameters of the PBCF and NBCF oxides are listed in Table 1. It can be seen that lattice parameters and unit-cell volumes decrease from PBCF to NBCF. According to iodometric titration results, the nonstoichiometric δ values of oxygen in the PBCF and NBCF oxides are 0.79 and 0.67, respectively. This finding is in agreement with Klyndyuk et al. [30,32]. It is generally believed that the oxygen vacancy could result in an increase of unit-cell volume due to the reduction of the smaller-ionic size Co⁴⁺ to larger-ionic size Co³⁺. However, the decreasing size of the rare earth cations Ln³⁺ plays a predominant role in controlling overall unit-cell volume [6]. The ionic radius of Pr is larger than that of Nd [33]; therefore, the unit-cell volume of LnBCF decreases from PBCF to NBCF. In addition, the substitution of Fe for Co is also found to increase the unit-cell volume of PBCF and NBCF as compared to the undoped LnBaCo₂O_{5+ δ} [9,11,25]. This is because ionic radii of Fe^{3+/4+} are larger than those of Co^{3+/4+} [33], leading to an increase in unit-cell volume.

Chemical compatibilities between cathode and electrolyte were examined. The PBCF and NBCF cathodes with LSGM electrolyte were mixed in a weight ratio of 1:1 and calcined at 1000 °C for 10 h in air. Fig. 1(c) and (d) shows the XRD patterns of the PBCF-LSGM and NBCF-LSGM mixtures after heat treatment. It is clear that diffraction peaks of only PBCF-LSGM and NBCF-LSGM are present, with no other impurities. No obvious diffraction peak shifts are observed in the XRD patterns. These results suggest no apparent chemical reaction occurs between the LnBaCoFeO_{5+ δ} cathodes and LSGM electrolyte up to 1000 °C. Furthermore, a chemically stable cathode material for LSGM electrolyte-based SOFCs is necessary to ensure a good connection.

3.2. SEM and EDS analysis

In this study, SEM is used for microstructural observation and EDS for quantitative elemental analysis of materials. Fig. 2 shows the SEM micrographs of the PBCF and NBCF samples sintered at 1150 °C for 10 h. The particle sizes of the two samples are similar, but the sintered densities are very different: the PBCF sample is dense and the NBCF sample is porous. This indicates that sintering at 1150 °C for 10 h is a suitable treatment for PBCF, but not for NBCF. On further investigation, it was found that sintering at 1200 °C for 10 h gives dense NBCF samples (see Section 3.5).

EDS results of the PBCF and NBCF samples are listed in Table 2. Each sample has five detectable elements (Pr/Nd, Ba, Co, Fe, and O). These metal elements are present in approximately 1:1:1:1 molar ratio, indicating that the element contents of the PBCF and NBCF materials synthesized in this study accord quite well with the nominal stoichiometric index.

3.3. XPS analysis

Fig. 3 shows the survey XPS spectra of the PBCF and NBCF samples. The characteristic lines of the Pr, Nd, Ba, Co, Fe, and O are present. The binding energies of observed peaks were normalized with a C1s peak to 284.6 eV and quoted with a precision of ± 0.2 eV.

Table 1
Unit-cell parameters of PBCF and NBCF samples.

Samples	Lattice parameters		Volume (\AA^3)
	<i>a</i> (\AA)	<i>c</i> (\AA)	
PBCF	3.9184	7.6568	117.56
NBCF	3.9090	7.6252	116.52

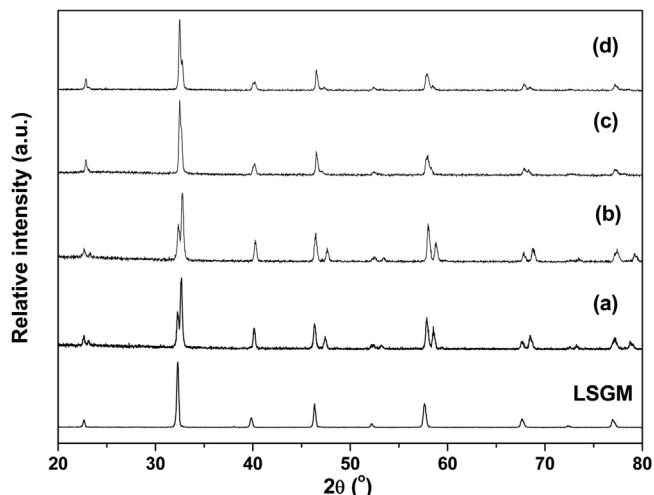


Fig. 1. XRD patterns of samples: (a) PBCF and (b) NBCF sintered at 1150 °C for 10 h in air; (c) PBCF-LSGM and (d) NBCF-LSGM mixtures calcined at 1000 °C for 10 h in air; LSGM sintered at 1450 °C for 10 h in air.

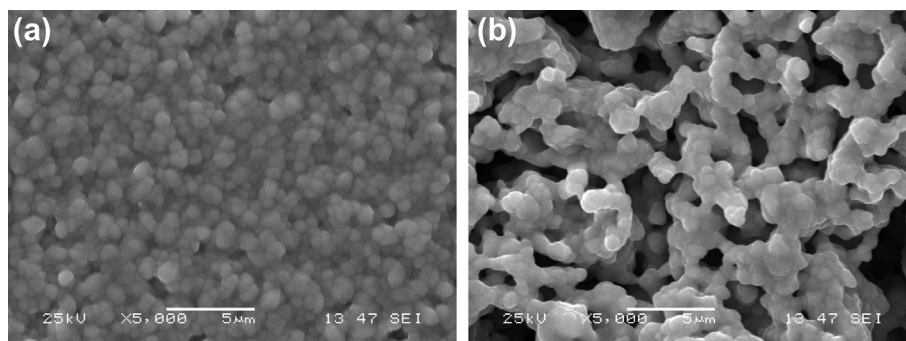


Fig. 2. SEM micrographs of samples sintered at 1150 °C for 10 h in air: (a) PBCF and (b) NBCF.

To identify the chemical state of rare earth and transition metal cations, the XPS of the Pr 3d, Nd 3d, Fe 2p, and Co 2p in the PBCF and NBCF samples are discussed in detail below. Fig. 4 shows the Pr 3d and Nd 3d spectra of the PBCF and NBCF. It is clear from Fig. 4(a) that the Pr 3d_{5/2} and Pr 3d_{3/2} spectra each contain three distinguishable peaks. The 3d_{5/2} peaks, located at 927.9 and 933.0 eV, can be assigned to the Pr³⁺ cation, whereas the weak satellite peak with binding energy of 931.0 eV can be attributed to the Pr⁴⁺ cation. This result is consistent with evidence from the literature [29,34]. It is noteworthy that peaks assigned to Pr³⁺ are stronger than the peak of Pr⁴⁺, indicating that the oxidation state of Pr³⁺ is dominant in the PBCF. Fig. 4(b) shows the XPS results of the Nd 3d spectra for the NBCF. The Nd 3d_{5/2} and 3d_{3/2} peaks are clearly distinguishable at binding energies of 983.2 and 1005.7 eV, and the binding energy separation between the 3d_{5/2} and Nd 3d_{3/2} states is around 22.5 eV, suggesting that there is only one oxidation state of the Nd³⁺ cation. The binding energy results are in good agreement with literature data [35,36].

Fig. 5 shows the Fe 2p XPS spectra of the PBCF and NBCF samples. The Fe 2p_{3/2} and 2p_{1/2} peaks appear at around 709.5–709.7 eV and 722.8–723.1 eV, respectively, indicating the existence of Fe³⁺ species. Another set of doublet peaks, observed at around 711.3–711.4 eV and 724.1–724.4 eV, can be assigned to Fe⁴⁺ species [29,37]. Two satellite peaks with binding energies of 717.8 eV (Fig. 5(a)) and 715.2 eV (Fig. 5(b)) can be attributed to Fe³⁺ species.

Fig. 6 shows the Co 2p XPS spectra of the PBCF and NBCF samples. Spin-orbit splitting of Co at 2p_{3/2} and 2p_{1/2} is clearly distinguishable due to the existence of mixed valence states of Co³⁺ and Co⁴⁺. The Co³⁺ 2p_{3/2} and 2p_{1/2} core-level fitting spectra present two components at around 778.9–778.4 eV and 793.4–793.5 eV, whereas the Co⁴⁺ 2p_{3/2} and 2p_{1/2} core-level fitting spectra display two components at around 780.8–780.4 eV and 795.2–795.4 eV [29,38]. It should be noted that the satellite peaks at around 787.5 ± 0.5 eV are not detected in any XPS spectra, suggesting the absence of Co²⁺ [39].

Table 2
EDS results of PBCF and NBCF samples.

Samples	Metal elements	wt%	at%	Elemental ratio (EDS results)	Elemental ratio (nominal values)
PBCF	Pr	31.7	12.5	1.033	1.000
	Ba	30.0	12.4	1.025	1.000
	Co	11.9	11.4	0.942	1.000
	Fe	11.9	12.1	1.000	1.000
NBCF	Nd	33.3	13.2	1.088	1.000
	Ba	29.5	12.3	1.014	1.000
	Co	11.6	11.4	0.941	1.000
	Fe	11.3	11.6	0.957	1.000

From the XPS spectra of the Pr 3d, Nd 3d, Ba 3d, Fe 2p, and Co 2p, the integrated intensity ratios of the Pr⁴⁺/Pr³⁺, Nd³⁺, Ba²⁺, Fe⁴⁺/Fe³⁺, and Co⁴⁺/Co³⁺ were calculated and are shown in Fig. 7. For the PBCF sample, Pr³⁺ concentration is much higher than that of Pr⁴⁺. The Nd and Ba ions are thoroughly occupied, as indicated by the single-valence state of +3 and +2, respectively. It is interesting to note that the Fe⁴⁺/Fe³⁺ and Co⁴⁺/Co³⁺ ratios increase with a change from PBCF to NBCF. For example, the respective ratios of Fe⁴⁺/Fe³⁺ and Co⁴⁺/Co³⁺ are 57/44 and 64/36 in PBCF, while these values are 60/40 and 71/29 in NBCF. Obviously, according to electrical neutrality, the existence of Pr⁴⁺ cations results in a decrease in the ratio of Fe⁴⁺/Fe³⁺ and Co⁴⁺/Co³⁺ in PBCF.

The presence of mixed valence excites a number of carriers, causing a p-type conducting mechanism, which is demonstrated by the conductivity measurements below. The reduction from high-valence state cations to low-valence state results in the formation of oxygen vacancies with increasing temperature, which is demonstrated by the TGA data in Section 3.4. These oxygen vacancies are beneficial to enhance the permeation, adsorption, and activation of oxygen, thus improving the oxide-ion conductivity and electrochemical catalytic activity for oxygen reduction. Therefore, the mixed valence Pr⁴⁺/Pr³⁺, Co⁴⁺/Co³⁺, and Fe⁴⁺/Fe³⁺ redox couples play an important role in the conduction and electrochemical performance of PBCF and NBCF cathodes.

3.4. Thermal expansion behavior

Fig. 8 shows the thermal expansion and thermal expansion coefficient (TEC) curves of the PBCF and NBCF samples measured

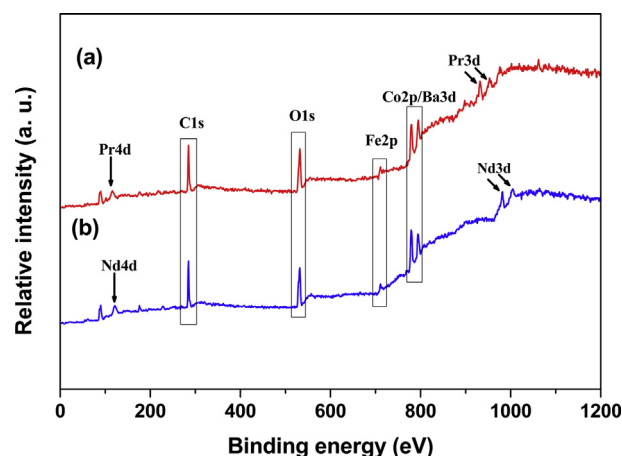


Fig. 3. Survey XPS spectra of samples at room temperature: (a) PBCF and (b) NBCF.

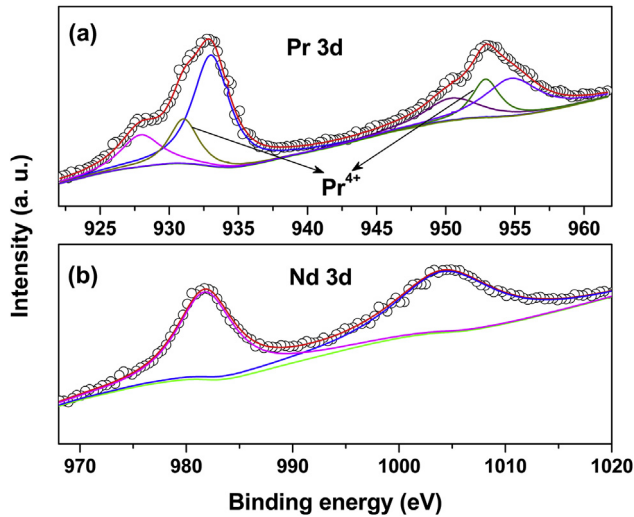


Fig. 4. Ln 3d core-level spectra of samples at room temperature: (a) PBCF and (b) NBCF.

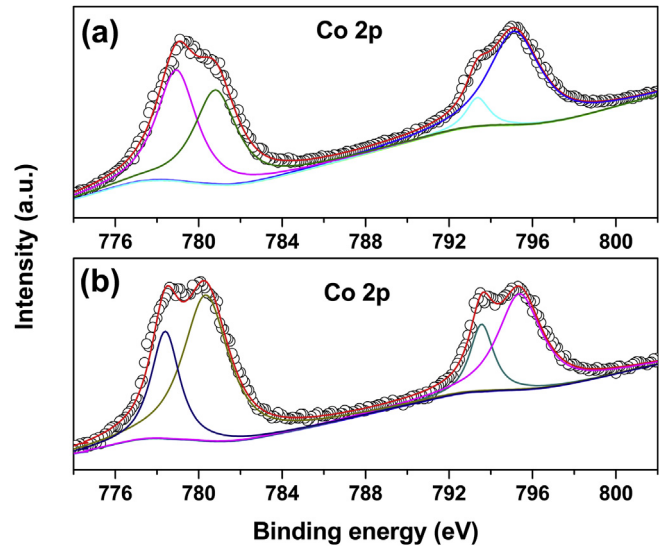
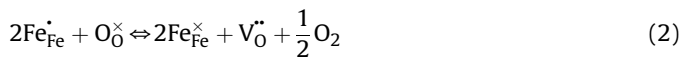
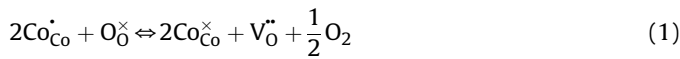
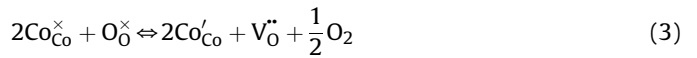


Fig. 6. Co 2p core-level spectra of samples at room temperature: (a) PBCF and (b) NBCF.

between 30 and 1000 °C in air. It can be seen that the slope of the thermal expansion curves changes at around 300 °C, which is related to the formation of the oxygen vacancies and the reduction of the Fe/Co cations from higher to lower valences [6,11]. The defect reactions can be expressed in the following equations:



The thermal expansion curves of the PBCF and NBCF samples are almost linear from 300 to 1000 °C, which indicates that there are no crystal structure transitions in the temperature range. However, a small variation at about 880 °C appears in both TEC curves. This can be attributable to the thermal reduction of the trivalent state $\text{Co}^{3+}/\text{Fe}^{3+}$ to divalent state $\text{Co}^{2+}/\text{Fe}^{2+}$ and is accompanied by further formation of oxygen vacancies [40]. The defect formation can be described in Eq. (3):



The average TEC values of the PBCF and NBCF samples are $21.0 \times 10^{-6} \text{ K}^{-1}$ and $19.5 \times 10^{-6} \text{ K}^{-1}$, respectively, in temperature range 30–1000 °C. Obviously, these values are lower than those of the $\text{LnBaCo}_2\text{O}_{5+\delta}$ (Ln = Pr and Nd) cathode materials, which are $21.5 \times 10^{-6} \text{ K}^{-1}$ and $21.0 \times 10^{-6} \text{ K}^{-1}$ [14]. The Fe–O bond is stronger than the Co–O bond, resulting in a decreased TEC of the $\text{LnBaCo}_{2-x}\text{Fe}_x\text{O}_{5+\delta}$ with increasing Fe content [9]. Therefore, substitution of Fe for Co reduces the TECs for the PBCF and NBCF samples. It is noted, as in the case of other cobalt-based perovskite cathode materials, that the TEC values of the PBCF and NBCF materials are still higher than those of common electrolyte materials such as SDC and LSGM, which are 11.4×10^{-6} and $11.5 \times 10^{-6} \text{ K}^{-1}$ in the temperature range of 30–1000 °C [24]. An approach that introduces the SDC electrolyte to form composite cathodes is under consideration to further reduce average TEC of PBCF and NBCF materials.

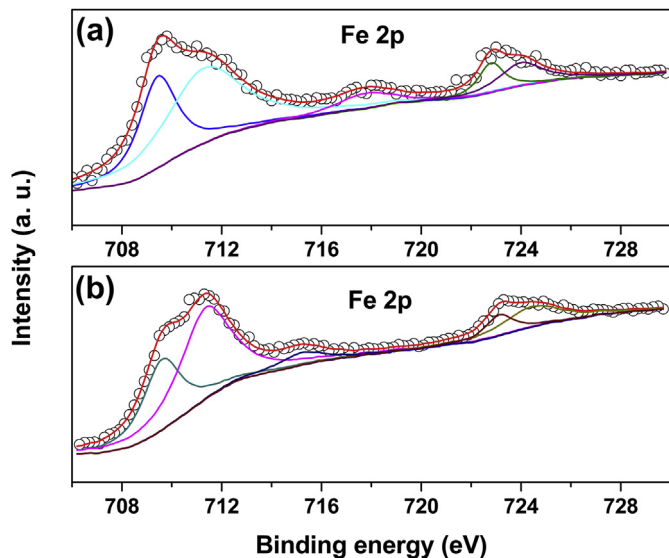


Fig. 5. Fe 2p core-level spectra of samples at room temperature: (a) PBCF and (b) NBCF.

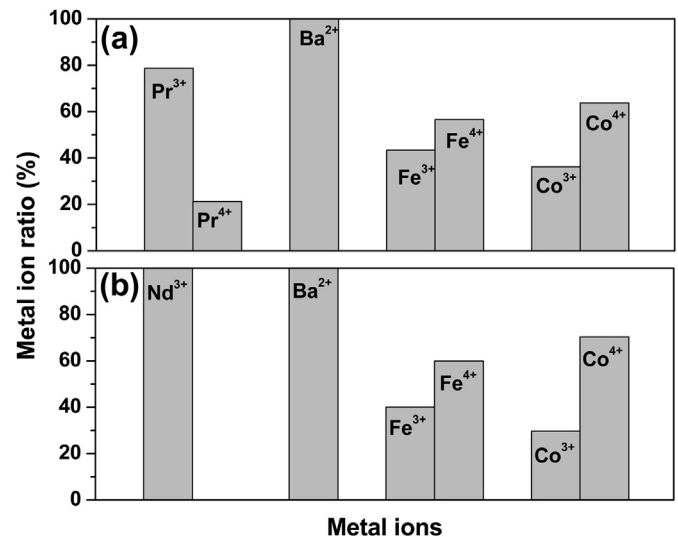


Fig. 7. Atomic ratio of $\text{Pr}^{3+}/\text{Pr}^{4+}$, Nd^{3+} , Ba^{2+} , $\text{Fe}^{3+}/\text{Fe}^{4+}$, and $\text{Co}^{3+}/\text{Co}^{4+}$: (a) PBCF and (b) NBCF.

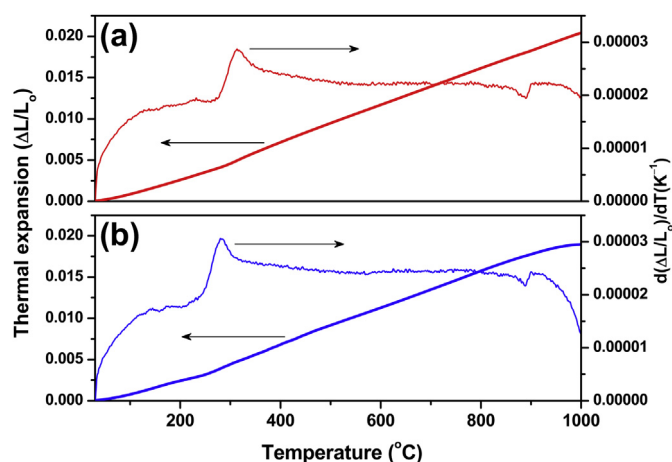


Fig. 8. Thermal expansion behaviors of samples between 30 and 1000 °C in air: (a) PBCF and (b) NBCF.

3.5. TGA

To reveal the change of oxygen vacancies with temperature, we measured the TGA curves of the samples. Fig. 9(a) compares the variation of weight of the PBCF and NBCF samples with temperature upon heating. The TGA curves of the two samples are similar: they show a slow weight loss at a temperature below about 300 °C. This is mainly due to desorption of moisture and carbon dioxide. The TGA curves display a rapid weight loss beyond 300 °C; this can be attributed to the loss of weakly bound lattice oxygen, which corresponds to the formation of oxygen vacancies and the reduction of $\text{Co}^{4+}/\text{Fe}^{4+}$ to $\text{Co}^{3+}/\text{Fe}^{3+}$ as described in equations (1) and (2). In addition, it is observed that PBCF experiences more weight loss than NBCF with increasing temperature, suggesting that the binding energy between oxygen ions and rare earth ions in the lattice increases with decreasing ionic radius of Ln. A similar phenomenon was observed in $\text{Ln}_{0.6}\text{Sr}_{0.4}\text{CoO}_{3-\delta}$ perovskite materials by Lee and Manthiram [41]. Compared with NBCF, PBCF has a larger oxygen weight loss, indicating that it has higher oxygen diffusion and surface exchange kinetics.

Fig. 9(b) shows the variation of oxygen content in the samples with temperature when they are heated in air. It can be seen that the oxygen content decreases with increasing temperature due to a

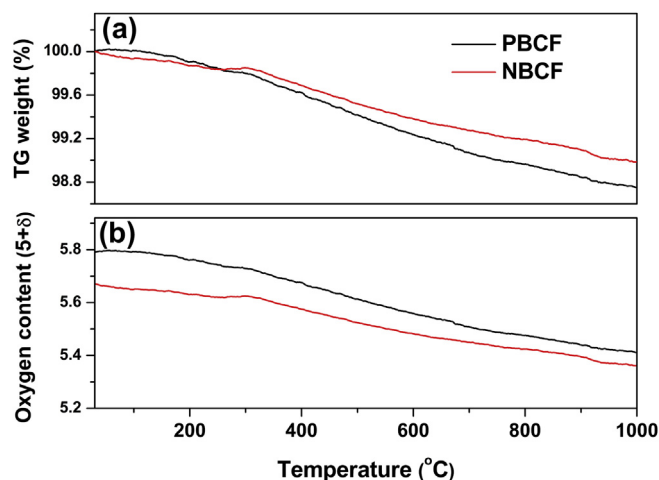


Fig. 9. (a) TGA curves and (b) variations of oxygen content of PBCF and NBCF samples with temperature in air.

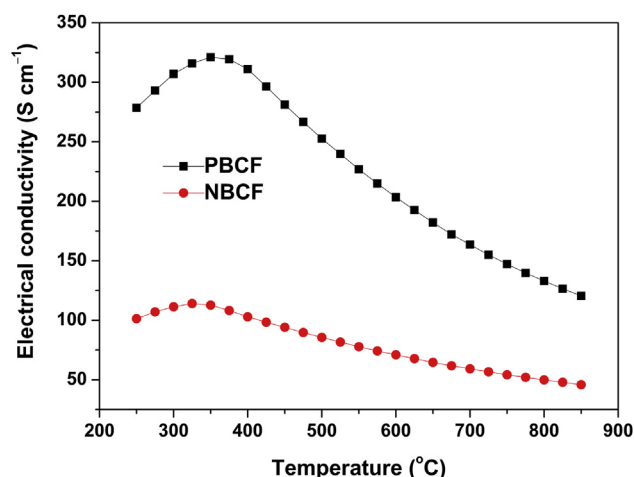


Fig. 10. Temperature dependence of electrical conductivity of PBCF and NBCF samples sintered at 1150 °C for 10 h in air.

partial loss of lattice oxygen. The oxygen content in the NBCF sample is less than that in the PBCF sample, as shown in Fig. 9(b). Kim and Prado [42] have investigated the variations of the oxygen contents ($5 + \delta$) with the difference in ionic radii between Ba^{2+} and Ln^{3+} in the $\text{LnBaCo}_2\text{O}_{5+\delta}$ system. Their results showed that the increase in the ionic size difference between Ba^{2+} and Ln^{3+} could result in a decrease in the oxygen content, as Ln^{3+} tended to have fewer than 12 coordination bonds. Therefore, the oxygen content in the PBCF sample is more than that in the NBCF sample. Another reason is that the larger Pr ions possessed a greater number of oxygen atoms in the PBCF perovskite material [10].

3.6. Electrical conductivity

Fig. 10 shows the electrical conductivities of the PBCF and NBCF samples sintered at 1150 °C for 10 h in air. Being a mixed conductor, the total electrical conductivities of the PBCF and NBCF samples consist of electronic and the oxygen ionic conductivities. Ionic conductivity is generally several orders of magnitude lower than electronic conductivity; therefore, the measured conductivity values for the PBCF and NBCF samples mainly refer to electronic conductivity. It can be seen from Fig. 10 that electrical conductivity

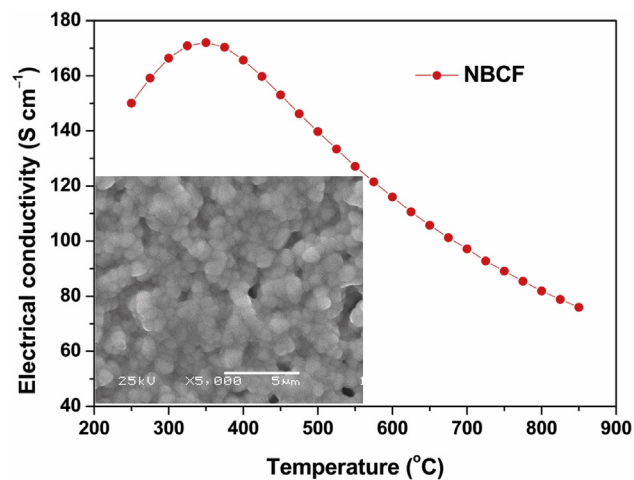


Fig. 11. Temperature dependence of electrical conductivity of NBCF sample sintered at 1200 °C for 10 h in air. Inset shows SEM micrograph of NBCF sample.

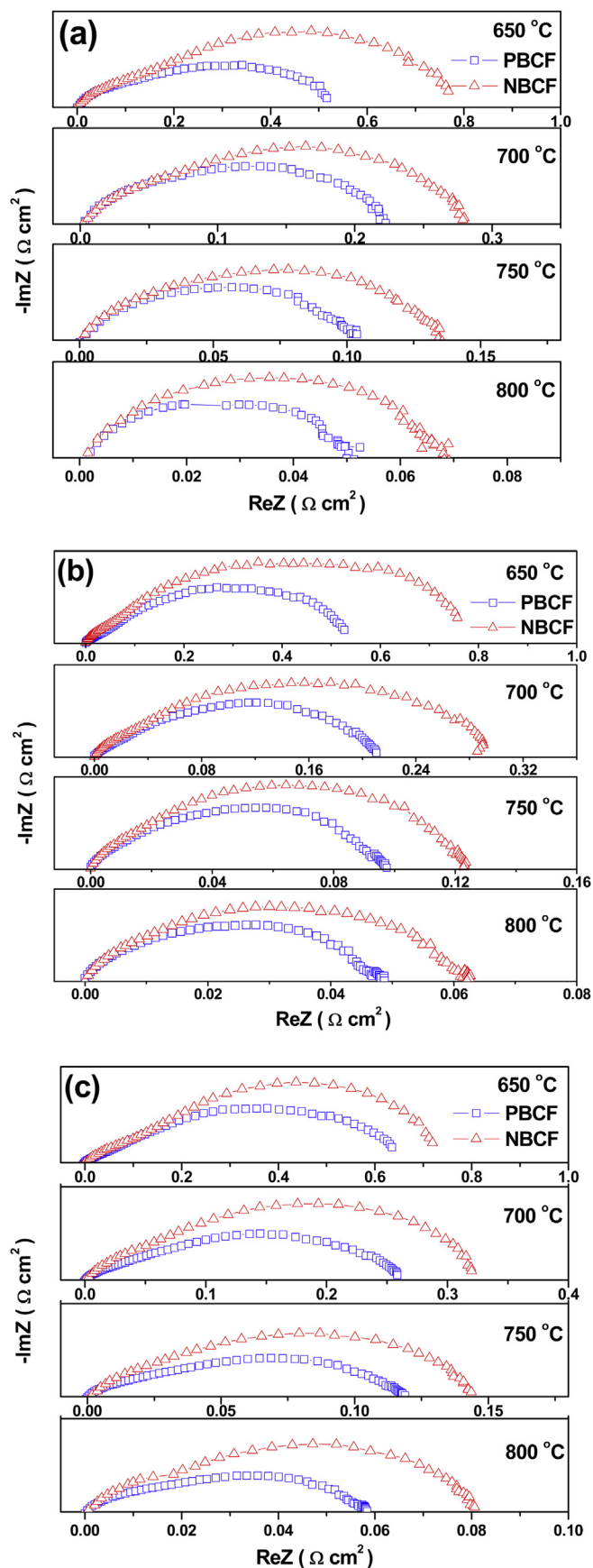


Fig. 12. Typical impedance spectra of PBCF and NBCF cathodes on LSGM electrolyte sintered at (a) 900 °C, (b) 950 °C, and (c) 1000 °C for 2 h in air. Ohmic resistance was subtracted from experimental data.

of the samples increases with temperature and reaches a maximum value at about 350 °C, showing a semiconductor-like behavior. Electrical conductivity begins to gradually decrease beyond 350 °C, exhibiting a metallic behavior. The increase in conductivity of the samples with increasing temperature below 350 °C is due to the hopping conduction mechanism of small polarons, where the localized electronic carriers are thermally activated [43]. The decrease in electrical conductivity beyond 350 °C can be attributed to the oxygen loss from the lattice. Meanwhile, some $\text{Co}^{4+}/\text{Fe}^{4+}$ ions are converted to $\text{Co}^{3+}/\text{Fe}^{3+}$ ions because of the charge neutrality, resulting in a reduced concentration of small polarons. Therefore, electrical conductivity decreases with increasing temperature. Similar conduction behaviors were also observed in $\text{PrBaCo}_{2-x}\text{Fe}_x\text{O}_{5+\delta}$ [11,12], $\text{LnBaCo}_{2-x}\text{Fe}_x\text{O}_{5+\delta}$ ($\text{Ln} = \text{Nd}$ and Gd) [9], and $\text{LaSr}_3\text{Fe}_{3-y}\text{Co}_{10-\delta}$ [44] systems.

We can see from Fig. 10 that the PBCF sample has a higher electrical conductivity (321 S cm^{-1}) at 350 °C in air compared to the NBCF sample (114 S cm^{-1}). The electrical conductivity of the samples decreases from $\text{Ln} = \text{Pr}$ to Nd within the studied temperature range due to the increasing oxygen vacancy concentration and bending of the O–Co–O bonds [6]. The increase of oxygen vacancy concentration not only decreases the charge carrier concentration but also perturbs the (Co, Fe)–O–(Co, Fe) periodic potential and results in carrier localization [6,9,14]. Therefore, the electrical conductivity of the $\text{LnBaCoFeO}_{5+\delta}$ samples decreases from $\text{Ln} = \text{Pr}$ to Nd . In addition, as shown by the SEM micrographs in Fig. 2, the PBCF sample has a highly dense microstructure, while the NBCF sample has a porous microstructure. This is another reason the electrical conductivity of the PBCF sample is higher than that of the NBCF sample.

Compared to other double perovskite cathodes, electrical conductivities of the PBCF sample are significantly higher than those of the $\text{GdBaCoCuO}_{5+\delta}$ [24] and $\text{PrBaCoCuO}_{5+\delta}$ [26] samples. However, the electrical conductivities of the PBCF and NBCF samples are lower compared to the $\text{LnBaCo}_2\text{O}_{5+\delta}$ ($\text{Ln} = \text{Pr}$ and Nd) [14]. This is because the substitution of Fe for Co in $\text{LnBaCoFeO}_{5+\delta}$ materials disrupts the $\text{Co}^{4+}\text{--O}^{2-}\text{--Co}^{3+}$ conduction path and hinders electron hopping [45], resulting in a decrease of electrical conductivity. Electrical conductivity values of the PBCF and NBCF samples are, respectively, 203–133 and 71–50 S cm^{-1} between 600 and 800 °C in air.

In order to more accurately measure the electrical conductivity of the NBCF sample, dense NBCF was obtained by sintering the sample at 1200 °C for 10 h. Fig. 11 shows the temperature dependence of the electrical conductivity of the NBCF sample sintered at 1200 °C for 10 h in air; the inset is the SEM micrograph of the NBCF sample. We can see that the dense NBCF sample has been prepared after sintering at 1200 °C for 10 h. The electrical conductivity of the NBCF sample also shows a p-type semiconductor behavior at low temperature and changes to metallic behavior at high temperature, which is in good agreement with the PBCF and NBCF samples sintered at 1150 °C for 10 h. The electrical conductivity of the NBCF sample reaches a maximum of 172 S cm^{-1} at 350 °C.

3.7. Impedance analysis

Fig. 12(a)–(c) shows the typical impedance spectra of the symmetrical cells using PBCF and NBCF as cathodes on LSGM electrolyte sintered at different temperatures in air. The impedance spectra data have been normalized to zero by deducting the ohmic resistances. The impedance spectra show the two arcs on the complex plane, suggesting there are at least two electrode processes corresponding to the high- and low-frequency arcs. The impedance spectra were fitted to an equivalent circuit by using the Z-view software as depicted in reference [46]. The area specific resistances (ASRs, polarization resistances) are calculated from the difference between the

high-frequency and low-frequency intercepts on the real axis. Comparison of the EIS results indicates that the PBCF and NBCF cathodes on LSGM electrolyte sintered at 950 °C for 2 h have the smallest ASR values at all sintering temperatures, which can be related to the cathode microstructures (porosity, particle surface area, and connection) and contact between the cathode and electrolyte. This suggests that a sintering temperature of 950 °C is the optimal selection for maintaining good microstructures and interfacial adhesion between the cathode and electrolyte. Therefore, electrochemical performances of the PBCF and NBCF cathodes on LSGM sintered at 950 °C for 2 h are discussed in the following section.

We can see from Fig. 12(b) that the ASR values decrease with increasing temperature. ASR values of the PBCF cathode are as low as 0.049 $\Omega \text{ cm}^2$ at 800 °C and 0.098 $\Omega \text{ cm}^2$ at 750 °C; for the NBCF cathode, the ASR values are 0.062 and 0.119 $\Omega \text{ cm}^2$ at 800 and 750 °C, respectively. Thus, the ASR values of the PBCF cathode are lower than those of the NBCF cathode. The diffusion coefficient and surface exchange coefficient decrease as the radius of Pr^{3+} is larger than that of Nd^{3+} , and the cathode materials containing Pr^{3+} have higher electrical conductivity and lower overpotential values because of the $\text{Pr}^{3+}/\text{Pr}^{4+}$ valence change [18,47]. Moreover, the ASR values are lower than that of previously reported LnBCF cathodes for SOFC. For example, Lü et al. [48] reported that the ASR of the $\text{SmBaCoFeO}_{5+\delta}$ cathode on GDC electrolyte is 0.1 $\Omega \text{ cm}^2$ at 800 °C. However, the ASR values of the PBCF and NBCF cathodes are slightly larger than those of the $\text{LnBaCo}_2\text{O}_{5+\delta}$ (Ln = Pr and Nd) cathodes, where the ASR values are 0.070 $\Omega \text{ cm}^2$ and 0.093 $\Omega \text{ cm}^2$ at 700 °C for Ln = Pr and Nd [14], respectively. This is largely because the

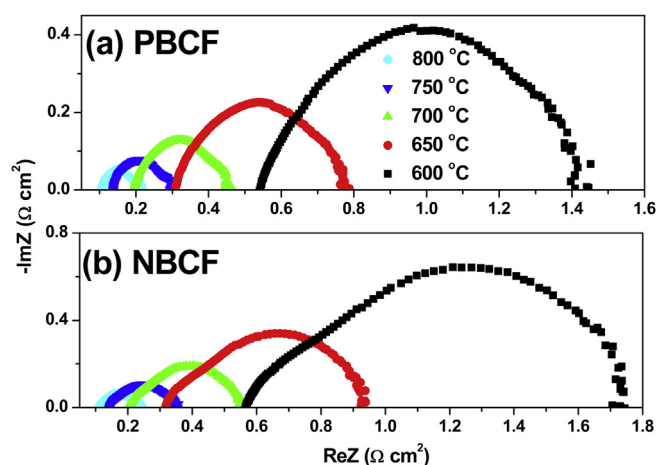


Fig. 14. Typical impedance spectra of single cells with PBCF and NBCF cathodes measured at different temperatures under open-circuit conditions.

electrocatalytic property of Co for oxygen reduction is higher than that of Fe. A similar behavior was also observed in $\text{YBaCo}_{2-x}\text{Fe}_x\text{O}_{5+\delta}$ cathodes [49]. The PBCF and NBCF cathode performances are slightly lower than those of $\text{LnBaCo}_2\text{O}_{5+\delta}$ (Ln = Pr and Nd), but they still retain better electrochemical performances (Fig. 12(b)). In addition, introducing electrolyte material into the cathode to form a composite cathode would further improve the PBCF and NBCF cathode performances.

3.8. Single-cell performance

To further identify the properties of the PBCF and NBCF as cathode materials, electrolyte-supported Ni-SDC/SDC/LSGM/LnBCF cell performances were tested. Fig. 13 shows the variation of cell voltage and power density as a function of current density with H_2 as the fuel and ambient air as the oxidant. It can be seen that the maximum power densities at 800 °C are 749 and 669 mW cm^{-2} for the PBCF and NBCF cathodes, respectively. The cell power density is higher with the PBCF cathode than with the NBCF cathode, which is in agreement with the electrical conductivity and the ASR results mentioned above. Fig. 14 shows the EIS of single cells measured at different temperatures. The total ASR values of single cells at 800 °C are 0.106 and 0.127 $\Omega \text{ cm}^2$ for the PBCF and NBCF cathodes, respectively. The results are in agreement with those of symmetrical cells. Compared to other double perovskite cathodes, the PBCF and NBCF cathodes exhibit a much better performance under similar conditions. For example, the power density of the Ni-GDC/GDC/ $\text{SmBaCoFeO}_{5+\delta}$ cell reached only 431 mW cm^{-2} at 800 °C [48], and the cell power density with a $\text{GdBaCoCuO}_{5+\delta}$ cathode on LSGM electrolyte was 545 mW cm^{-2} at 800 °C [24]. The results indicate that the double perovskite PBCF and NBCF cathodes on LSGM electrolyte exhibit excellent electrochemical performances, indicating they are suitable for use as LaGaO_3 -based IT-SOFC cathodes.

4. Conclusions

The double perovskites PBCF and NBCF are prepared and assessed as potential cathode materials for IT-SOFCs on LSGM electrolyte. Micro-area chemical analysis indicates that the PBCF and NBCF materials with metal stoichiometry ratios of about 1:1:1 are successfully achieved. The PBCF and NBCF materials have good chemical compatibility with the LSGM electrolyte at temperatures below 1000 °C. XPS studies indicate that the Pr cation is present as both Pr^{3+} and Pr^{4+} in PBCF and the Pr^{3+} state is

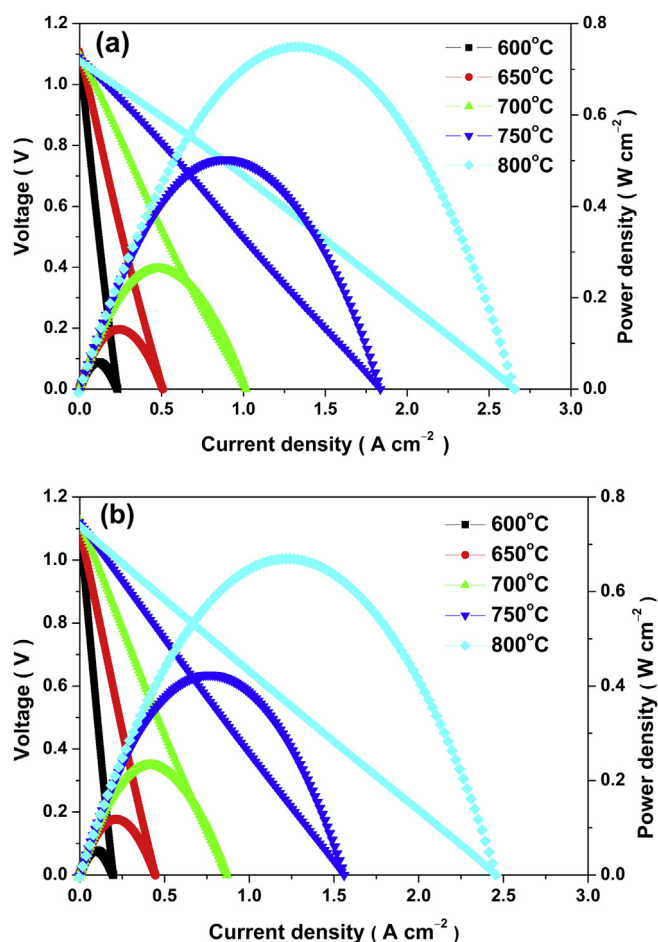


Fig. 13. Cell performance with H_2 as the fuel and ambient air as the oxidant at different temperatures: (a) PBCF and (b) NBCF cathodes.

dominant; whereas the Nd cation is present as Nd^{3+} in NBCF. $\text{Fe}^{3+}/\text{Fe}^{4+}$ and $\text{Co}^{3+}/\text{Co}^{4+}$ states coexist in these two compounds. Compared to $\text{LnBaCo}_2\text{O}_{5+\delta}$ materials, the partial substitution of Fe for Co reduces the TECs of the PBCF and NBCF materials. PBCF and NBCF materials on LSGM electrolyte sintered at 950°C 2 h show the best cathode performance: ASRs of the PBCF and NBCF cathodes on LSGM electrolyte at 800°C are 0.049 and $0.062\ \Omega\ \text{cm}^2$, respectively, and the maximum power densities of the cell with $0.3\ \text{mm}$ -thick LSGM electrolyte at 800°C are 749 and $669\ \text{mW}\ \text{cm}^{-2}$ for the PBCF and NBCF cathodes, respectively. These results indicate that Fe-substituted PBCF and NBCF double perovskites are potential cathodes for SOFC applications. Furthermore, there is considerable scope for decreasing the high TECs of PBCF and NBCF by preparing a composite cathode to further improve cathode performance and make them more suited to practical applications.

Acknowledgments

This work was supported by the Natural Science Foundation of China under contract no. 10974065.

References

- [1] N.Q. Minh, J. Am. Ceram. Soc. 76 (1993) 563–588.
- [2] A.J. Jacobson, Chem. Mater. 22 (2010) 660–674.
- [3] S.B. Adler, Chem. Rev. 104 (2004) 4791–4844.
- [4] E. Ivers-Tiffée, A. Weber, D. Herbristrit, J. Eur. Ceram. Soc. 21 (2001) 1805–1811.
- [5] D.J.L. Brett, A. Atkinson, N.P. Brandon, S.J. Skinner, Chem. Soc. Rev. 37 (2008) 1568–1578.
- [6] J.-H. Kim, A. Manthiram, J. Electrochem. Soc. 155 (2008) B385–B390.
- [7] D.J. Chen, R. Ran, K. Zhang, J. Wang, Z.P. Shao, J. Power Sources 188 (2009) 96–105.
- [8] H.T. Gu, H. Chen, L. Gao, Y.F. Zheng, X.F. Zhu, L.C. Guo, Int. J. Hydrogen Energy 34 (2009) 2416–2420.
- [9] Y.N. Kim, J.H. Kim, A. Manthiram, J. Power Sources 195 (2010) 6411–6419.
- [10] K. Zhang, L. Ge, R. Ran, Z.P. Shao, S.M. Liu, Acta Mater. 56 (2008) 4876–4889.
- [11] L. Zhao, J.C. Shen, B.B. He, F.L. Chen, C.R. Xia, Int. J. Hydrogen Energy 36 (2011) 3658–3665.
- [12] J. Zou, J. Park, B. Kwak, H. Yoon, J. Chung, Solid State Ionics 206 (2012) 112–119.
- [13] Q.J. Zhou, T.M. He, Y. Ji, J. Power Sources 185 (2008) 754–758.
- [14] Q.J. Zhou, F. Wang, Y. Shen, T.M. He, J. Power Sources 195 (2010) 2174–2181.
- [15] S.Y. Yoo, J.Y. Shin, G. Kim, J. Mater. Chem. 21 (2011) 439–443.
- [16] A. Tarancón, J. Peña-Martínez, D. Marrero-López, A. Morata, J.C. Ruiz-Morales, P. Núñez, Solid State Ionics 179 (2008) 2372–2378.
- [17] J.H. Kim, L. Mogni, F. Prado, A. Caneiro, J.A. Alonso, A. Manthiram, J. Electrochem. Soc. 156 (2009) B1375–B1382.
- [18] G. Kim, S. Wang, A.J. Jacobson, L. Reimus, P. Brodersen, C.A. Mims, J. Mater. Chem. 17 (2007) 2500–2505.
- [19] A. Tarancón, S.J. Skinner, R.J. Chater, F. Hernández-Ramírez, J.A. Kilner, J. Mater. Chem. 17 (2007) 3175–3181.
- [20] A. Maignan, C. Martin, D. Pelloquin, N. Nguyen, B. Raveau, J. Solid State Chem. 142 (1999) 247–260.
- [21] C. Martin, A. Maignan, D. Pelloquin, N. Nguyen, B. Raveau, Appl. Phys. Lett. 71 (1997) 1421–1423.
- [22] J.C. Burley, J.F. Mitchell, S. Short, D. Miller, Y. Tang, J. Solid State Chem. 170 (2003) 339–350.
- [23] K. Asai, A. Yoneda, O. Yokokura, J.M. Tranquada, G. Shirane, K. Kohn, J. Phys. Soc. Jpn. 67 (1998) 290–296.
- [24] Q.J. Zhou, Y.C. Zhang, Y. Shen, T.M. He, J. Electrochem. Soc. 157 (2010) B628–B632.
- [25] V.A. Cherepanov, T.V. Aksenova, L.Y. Gavrilova, K.N. Mikhaleva, Solid State Ionics 188 (2011) 53–57.
- [26] S. Choi, J. Shin, G. Kim, J. Power Sources 201 (2012) 10–17.
- [27] H.P. Ding, X.J. Xue, Int. J. Hydrogen Energy 35 (2010) 4316–4319.
- [28] L.G. Cong, T.M. He, Y. Ji, P.F. Guan, Y.L. Huang, W.H. Su, J. Alloy Compd. 348 (2003) 325–331.
- [29] F.J. Jin, S. Yu, R. Wang, T.M. He, J. Power Sources 234 (2013) 244–251.
- [30] A.I. Klyndyuk, Inorg. Mater. 45 (2009) 942–945.
- [31] A.I. Klyndyuk, Y.A. Chizhova, Funct. Mater. 16 (2009) 17–23.
- [32] A.I. Klyndyuk, E.A. Chizhova, Inorg. Mater. 49 (2013) 319–324.
- [33] R.D. Shannon, Acta Crystallogr. A 32 (1976) 751–767.
- [34] C. Abate, V. Esposito, K. Duncan, J.C. Nino, D.M. Gattia, E.D. Wachsman, E. Traversaz, J. Am. Ceram. Soc. 93 (2010) 1970–1977.
- [35] F. Rivera-López, Mariano Pérez, Surf. Interface Anal. 44 (2012) 927–930.
- [36] B. Glorieux, R. Berjoan, M. Matecki, A. Kammouni, D. Perarnau, Appl. Surf. Sci. 253 (2007) 3349–3359.
- [37] M. Ghaffari, M. Shannon, H. Hui, O.K. Tan, A. Irannejad, Surf. Sci. 606 (2012) 670–677.
- [38] E. Meza, J. Ortiz, D. Ruíz-León, J.F. Marco, J.L. Gautier, Mater. Lett. 70 (2012) 189–192.
- [39] N.A. Merino, B.P. Barbero, P. Ruiz, L.E. Cadús, J. Catal. 240 (2006) 245–257.
- [40] Z.P. Shao, G.X. Xiong, J.H. Tong, H. Dong, W.S. Yang, Sep. Purif. Technol. 25 (2001) 419–429.
- [41] K.T. Lee, A. Manthiram, J. Electrochem. Soc. 153 (2006) A794–A798.
- [42] J.-H. Kim, F. Prado, J. Electrochem. Soc. 155 (2008) B1023–B1028.
- [43] J.W. Stevenson, T.R. Armstrong, R.D. Carneim, L.R. Pederson, W.J. Weber, J. Electrochem. Soc. 143 (1996) 2722–2729.
- [44] K.T. Lee, A. Manthiram, Chem. Mater. 18 (2006) 1621–1626.
- [45] K. Gaur, S.C. Verma, H.B. Lal, J. Mater. Sci. 23 (1988) 1725–1728.
- [46] Y. Shen, F. Wang, X. Ma, T.M. He, J. Power Sources 196 (2011) 7420–7425.
- [47] T. Ishihara, T. Kudo, H. Matsuda, Y. Takita, J. Electrochem. Soc. 142 (1995) 1519–1524.
- [48] S.Q. Lü, G.H. Long, Y. Ji, X.W. Meng, C.C. Sun, Int. J. Hydrogen Energy 35 (2010) 7930–7935.
- [49] J.F. Xue, Y. Shen, T.M. He, J. Power Sources 196 (2011) 3729–3735.